



Characterization of Multilayered Multipass Friction Stir Weld on ASTM A572 G50 Steel

Multilayered multipass friction stir welding was made on A572 G50 steel, resulting in improvement of mechanical properties and grain refinement in the stir zone

BY Y. C. LIM, S. SANDERSON, M. MAHONEY, X. YU, D. QIAO, Y. WANG, W. ZHANG, AND Z. FENG,

ABSTRACT

A multilayered multipass friction stir weld (MM-FSW) on ASTM A572 Grade 50 steel was characterized to understand its potential application for thick-section structures. The 15-mm-thick section was fabricated by stacking three steel plates and then friction stir welding the plates together in a total of five passes. The unique butt/lap joint configuration encountered in the multilayer weld was examined to understand the effect of tool rotation direction on the joint quality, especially the formation of hooking defect. Charpy V-notch impact toughness tests showed generally higher impact toughness energy for the stir zone than the base metal with a ductile fracture mode. The microhardness value was measured from 195 to 220 HV in the stir zone, while the base metal showed an average value of 170 HV. The microstructure in the stir zone and the adjacent heat-affected zone was quantified using optical and scanning electron microscopy (SEM) including electron backscatter diffraction (EBSD). The increased toughness and hardness were correlated with the refined microstructure in the stir zone, resulting from severe plastic deformation and subsequent dynamic recrystallization during friction stir welding.

KEYWORDS

- Friction Stir Welding • Multilayer • High-Strength Low-Alloy Steel
- Mechanical Properties • Microstructure

Introduction

Due to its advantages over conventional fusion welding, including low distortion and improved mechanical properties (Ref. 1), friction stir welding (FSW), a solid-state joining process, has experienced increasingly broad applications in relatively soft materials such as aluminum, magnesium, and copper alloys (Refs. 2–5).

With the rapid development of new tool materials, such as polycrystalline cubic boron nitride (PCBN) and tungsten-based alloys (Ref. 6), FSW has been recently applied to high-strength, high-temperature (or hard) materials, such as steel and Ti alloys (Refs. 1, 7–9). Thomas et al. (Ref. 8) were among the first to investigate the feasibility of FSW of both 12% chromium alloy and low-carbon (0.1%

C) steels evaluating mechanical properties and weld nugget morphologies. Similarly, Lienert and coworkers (Ref. 1) studied the joining of hot-rolled AISI 1018 mild steel (0.18% C) using FSW. Both researchers identified grain refinement in the stir zone (SZ) and improved weld mechanical properties as compared to parent steels (i.e., base metals). Furthermore, Fujii and colleagues (Ref. 9) researched the mechanical properties and microstructural evolution of friction stir welds in three carbon steels with different carbon contents (i.e., ultralow carbon, 0.12% C, and 0.34% C steels) using different welding conditions. Both alloy composition and temperature resulting from different welding conditions significantly affected the microstructure and mechanical properties in this study. Khodri et al. (Ref. 10) also evaluated microstructures and mechanical properties of a high-carbon steel (0.95% C) with different FSW parameters. Different process parameters were shown to affect the evolution of microstructures, resulting in different microhardness values and fracture modes. Finally, Taendl et al. (Ref. 11) studied FSW of a multilayered steel sheet composed of 15 alternating layers of austenitic stainless steel and a martensitic stainless steel roll-bonded to a total thickness of 1.2 mm. The softening of martensitic layers after welding was alleviated by postweld heat treat-

Y. C. LIM, X. YU, D. QIAO, Y. WANG, W. ZHANG, and Z. FENG (fengz@ornl.gov) are with Materials Science & Technology Division, Oak Ridge National Laboratory, Oak Ridge, Tenn. S. SANDERSON is with MegaStir Technologies LLC, Provo, Utah. M. MAHONEY is a consultant, Midway, Utah.

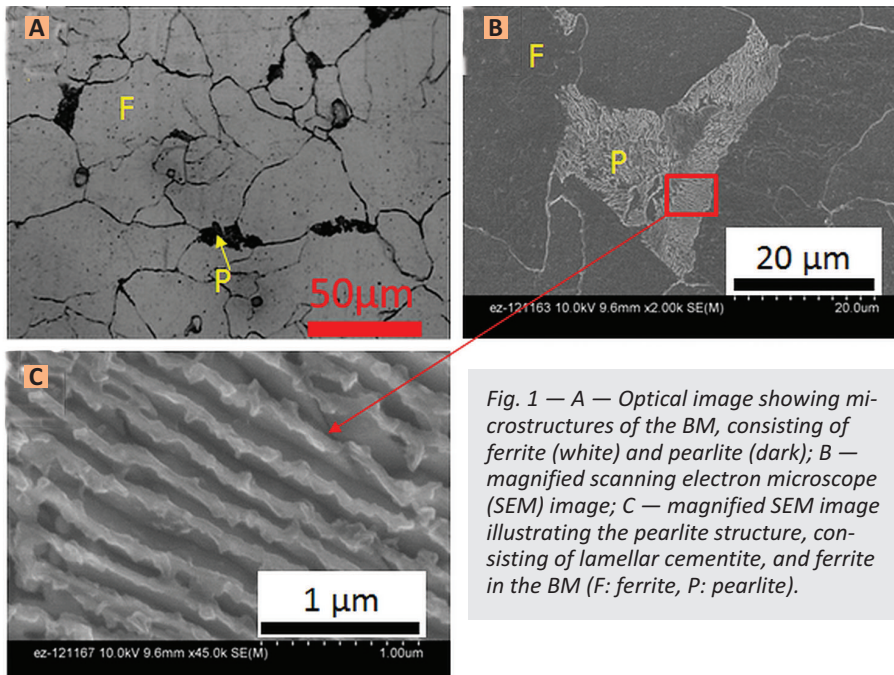


Fig. 1 — A — Optical image showing microstructures of the BM, consisting of ferrite (white) and pearlite (dark); B — magnified scanning electron microscope (SEM) image; C — magnified SEM image illustrating the pearlite structure, consisting of lamellar cementite, and ferrite in the BM (F: ferrite, P: pearlite).

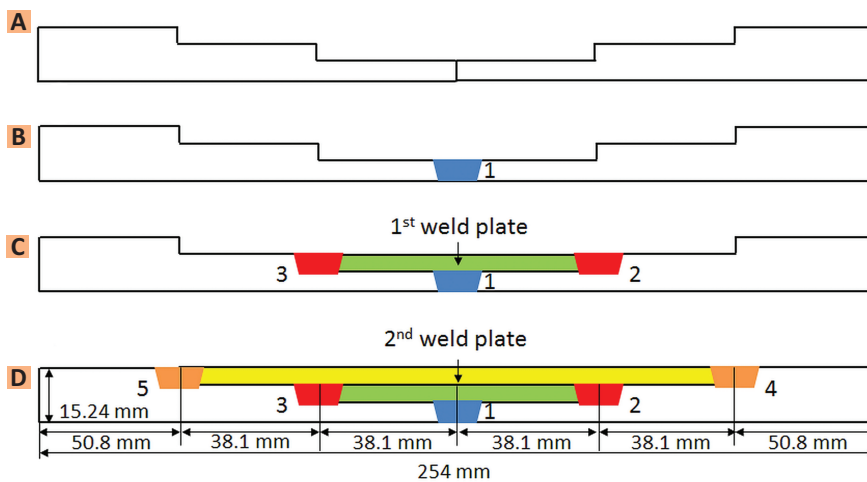


Fig. 2 — Cross sections showing A — Premachined A572 Grade 50 plate for MM-FSW; B — butt-joint weld for the bottom layer; C — insertion and FSW of the first weld plate above the root weld; D — insertion and FSW of the second weld plate above the first weld plate and the final welded structure. Thickness of both top and middle layers was 4.6 mm and the bottom layer was 6.1 mm. The total thickness of the MM-FSW structure was 15.2 mm. The combination of tool rotation direction (counter clockwise) and tool travel direction puts the advancing side of the weld at the lap interface.

ment to achieve 95% joint efficiency.

One shortcoming of FSW is the thickness of the workpiece that can be joined, especially for hard materials such as steels. That is, the length of the pin limits the thickness of material that can be friction stir welded. Only a few studies have reported FSW of steel plates thicker than 10 mm (Refs. 8, 12). Although double-sided welding has been attempted to make thick welds (up to 12 mm thick), it is still

difficult to make thick structures with a thickness greater than 15 mm. To overcome this limitation, a new method of FSW that can be applied to a thick section is needed.

A thick-section steel structure, fabricated by a novel multilayer and multipass FSW (MM-FSW) method, was demonstrated in the authors' recent work (Refs. 13, 14). Unlike the traditional multipass FSW (Ref. 15), the MM-FSW is based on a layer-by-layer

buildup approach to produce a thick structure with a conventional pin length.

In the present study, a friction stir welded multilayer structure of A572 Grade 50 steel, previously fabricated (Ref. 14), was characterized to understand its potential application for thick-section structures. In particular, the multilayered structure used corner joints; a unique joint configuration having both butt and lap features. Different tool rotation directions on the butt and lap joint configuration were applied and compared to understand the effect on friction stir weld quality especially the formation of hooking defect at the joint interface. Also, MM-FSW sample was characterized to understand the correlation between microstructure and mechanical properties. Specifically, optical and electron microscopy were used to understand the microstructural evolution in both the stir zone (SZ) and heat-affected zone (HAZ). Different regions in the friction stir welds were studied by electron backscatter diffraction (EBSD) for microstructural analysis and by micro-indentation test for hardness distribution. Charpy V-notch impact tests were performed in the SZ, HAZ, and base metal (BM) as a function of temperature. Fracture surfaces from the impact tests were evaluated by scanning electron microscopy (SEM) to assess the failure mode.

Experimental Methods

Friction Stir Welding Procedure

Detailed procedures for MM-FSW can be found in the authors' recent publication (Ref. 14). To provide the necessary background for the detailed characterization results (e.g., hooking defect and toughness) presented later, salient features of MM-FSW are described in the following:

A three-layered structure, with five multipass friction stir welds, was made using flat plates of high-strength low-alloy (HSLA) steel (ASTM A572 Grade 50; chemistry: 0.23C-1.35Mn-0.04P-0.05S-0.3Si-0.2Cu in wt-%) resulting in a total thickness of 15.2 mm. As shown in Fig. 1A, the base metal contains mainly equiaxed ferrite (F) and a small amount of pearlite (P). The mag-



Fig. 3 — Convex scroll shoulder step spiral pin (CS4 tool design) MS80 tool. The shoulder diameter was 36.8 mm with pin height and radius of 5.94 and 3.79 mm, respectively.

nified SEM image in Fig. 1B also indicates distinct ferrite and pearlite microstructures in the BM. Figure 1C shows the pearlite microstructure illustrating a lamellar structure consisting of alternate layers of ferrite and cementite. The width of the cementite lamellar layer was measured to be approximately 100 nm with a uniform spacing of slightly more than 100 nm. A brief description of each step for MM-FSW is illustrated in Fig. 2. A stepped assembly was machined to accommodate MM-FSW. To avoid overlapping with weld(s) in the previous layer, friction stir welds in the subsequent layer were offset transversely by a distance of 38.1 mm. For FSW, a tool with a convex scroll shoulder step spiral pin (CS4 tool design) was used and was fabricated from an MS80 grade of PCBN, as shown in Fig. 3. MS80 grade is a PCBN material made of Al-based ceramic binder phases with 80 vol-% of the ultrahard CBN phase. For FSW, the plunge was performed at 1100 rev/min followed by a 6-s dwell at 250 rev/min. Following the dwell, the tool rotation rate was maintained at 250 rev/min and the tool travel speed was $1.27 \text{ mm}\cdot\text{s}^{-1}$. The FSW was performed using load control with normal loads ranging from 32 to 35.6 kN.

Metallography and Hardness Testing

To reveal the microstructure at the weld zone for each layer, multilayered samples were cut and mounted for metallography. Diamond solutions (6, 3, and 1 μm) were used for final pol-

ishing of the mounted samples. A 5% Nital solution was used to etch the samples. An optical microscope (Nikon Epiphot) and field emission scanning electron microscope (FE-SEM) (Hitachi S4800) were used to characterize microstructures of the weld samples.

To characterize the original microstructure of the steel and the microstructural evolution in the SZ and HAZ, a JEOL 6500 scanning electron microscope equipped with an EBSD camera was used. This microscope has an accelerating voltage of 20 kV and a spot diameter of 5 nm with a scanning step size of 0.1 μm . EBSD maps were analyzed using OIM analysis software.

Vickers hardness of each welded sample was measured by a Leco microhardness tester (LM 100AT) with 200 μm spacing, 200 g of load, and 13 s of dwell time. The measured hardness data were transferred to *Origin*[®] software (*Origin Pro 8.1*) for visualizing hardness maps.

Charpy V-notch (CVN) impact toughness tests were conducted per ASTM E23 to study the fracture toughness of the SZ, HAZ, and BM at each of the three layers. Due to the different thicknesses at each layer, sub-sized samples were prepared for impact testing with the following dimensions ($10 \times 4 \times 55 \text{ mm}$) with the notch tip oriented parallel to the welding (or longitudinal) direction, as shown in Fig. 4. Charpy tests were performed at six different temperatures for the SZ, i.e., -50° , -30° , -20° , -10° , 0° , and 20°C . Similarly, samples located in the HAZ and BM were tested at -50° , 0° , and 20°C . Triplicate samples were tested at each temperature

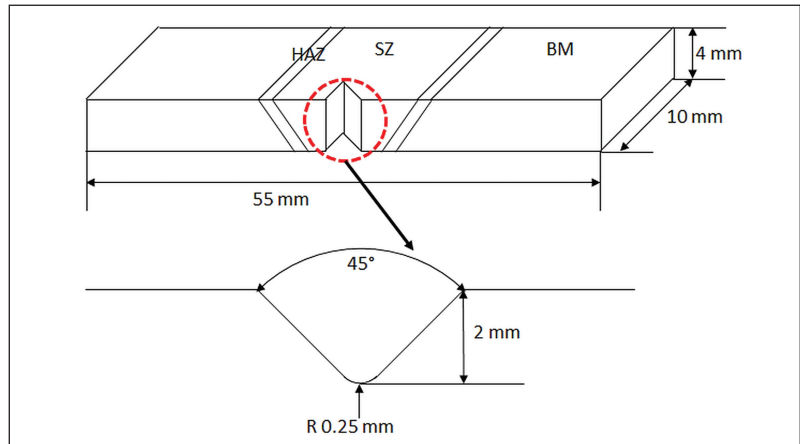


Fig. 4 — Notch location and dimensions of specimen for Charpy impact test.

at the Laboratory Testing Industry (LTI) facility. After Charpy impact tests, the fracture surfaces were studied by SEM imaging.

Results and Discussion

Characterization of MM-FSW Structure

One characteristic of MM-FSW is a combination of butt and lap joint configurations that involved inserting a metal plate to stack up the next layer. For this reason, it is referred to as a “butt/lap” joint. Such a butt/lap joint feature is likely to incur the interface defect called “hooking.” This defect is typically formed at a lap joint due to upward bending or flow of the metal horizontal interface when the tool penetrates into the bottom layer (Refs. 16–19). Figure 5 shows optical images at a butt/lap joint interface with two different process conditions. The first condition was with the FSW tool positioned on the retreating side of the lap interface, as shown in Fig. 5A. The latter condition positioned the FSW tool on the advancing side of the lap interface, as depicted in Fig. 5C. In the first condition, uplift of the interface occurred even though the weld nugget was free from volumetric defects, as shown in Fig. 5B. Conversely, Fig. 5D displays the top layer weld where interfacial hooking was minimized. That is, hooking was minimized by positioning the tool advancing side on the lap interface side of the corner joint. The difference in results is due to the difference in material flow

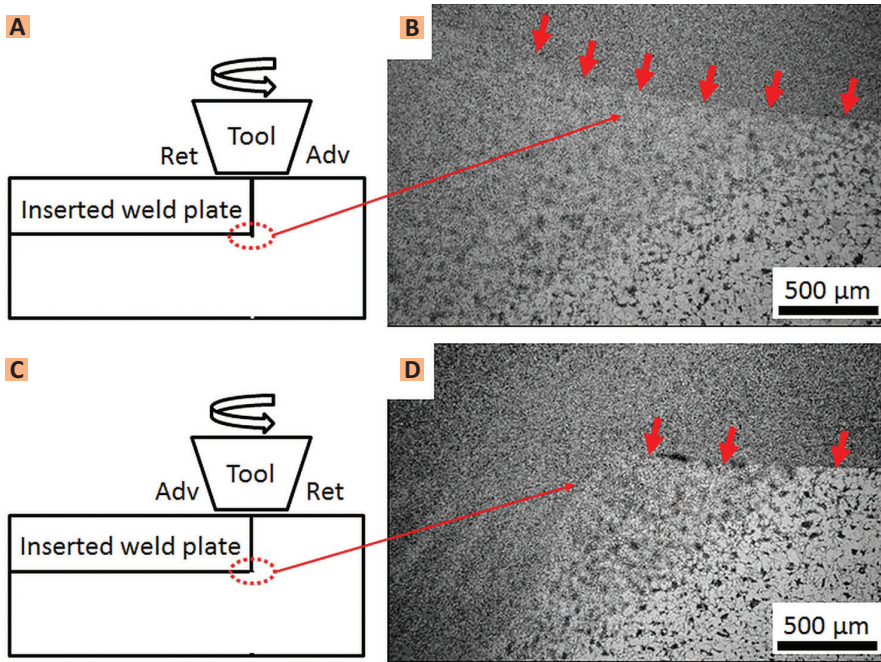


Fig. 5 — A — When the FSW tool was positioned with the retreating side located on the lap interface; B — optical image showing hooking defect at the lap interface (red color arrows); C — a corner weld with the FSW tool advancing side positioned on the lap interface; D — optical image showing minimal (or no) uplift of the lap interface. (Note: Adv is advancing side and Ret is retreating side.)

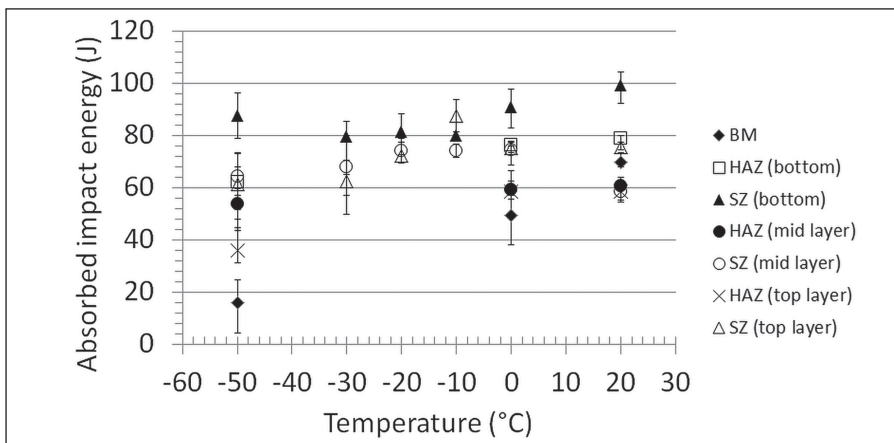


Fig. 6 — Charpy V-notch impact test results for each layer at different temperatures (Ref. 14).

caused by the different combinations of tool rotation direction and tool travel direction. The uplift of the lap interface in a corner joint is undesirable because it can result in a decrease in strength and potentially premature failure (Ref. 20). An alternative way to prevent a hooking defect is to use a specially designed lap joint tool, which has a feature at the tool tip that creates horizontal metal flow (Ref. 21), as opposed to threads or the step spiral that create vertical flow. With hori-

zontal metal flow, there is expected to be little uplift of the lap interface, thus minimizing hooking. This different approach is beyond the scope of work for the present paper.

Charpy Impact Toughness Test Result

Impact toughness of the SZ, HAZ, and BM of each layer was studied by Charpy V-notch impact tests at different temperatures. The Charpy impact

test results for each zone, with different layers at different test temperatures, are summarized in Fig. 6. For example, the average absorbed energy of the BM at the bottom layer (butt joint) was found to be 15.8 J at -50°C . The average impact toughness of the SZ at the bottom layer at -50°C was 87.7 J, i.e., almost 5.5 times higher than the BM. Toughness of the SZ at the bottom layer and the top layer was much higher than the BM at all tested temperatures. However, the absorbed energy of the SZ at the middle layer was higher for all temperatures up to 0°C but was lower at 20°C . One possible explanation is that the welds were not fully consolidated at this location, i.e., small voids and defects were observed in the SZ at the middle layer potentially lowering the impact toughness. In addition, the SZ at the top, middle, and bottom layers showed an average of 79.1, 74.1, and 81% shear fracture area. Next, the toughness of the HAZ at the bottom layer was 61.9 J, again considerably higher than the base metal at -50°C . The toughness of the HAZ at the top and middle layer was higher than the BM up to 0°C . The HAZ at top, middle, and bottom layers showed an average of 68.9, 68.9, and 78.3% shear fracture area. Konkol and Mruczek studied the toughness of friction stir welded HSLA-65 steel using subsized Charpy specimens (Ref. 22). They also found the toughness for the SZ and HAZ to be higher than the BM. Similar observations were obtained for aluminum alloys in previously reported studies (Refs. 23, 24). This substantial increase in the absorbed impact energy can be related to the fine grain size of the SZ and HAZ. The grain size of each zone is discussed below with the microstructure images. For comparison, the BM showed an average of 20, 72, and 80% shear fracture area at -50° , 0° , and 20°C test temperatures, respectively.

The SEM images, which illustrate fracture surfaces from the impact toughness tests for each zone at the bottom layer, are shown in Fig. 7. For the SZ, the failure mode at all temperatures was found to be ductile fracture with the presence of dimples at the fracture surface — Fig. 7A–C. Similarly, the fracture mode was ductile for the HAZ with dimples at the fracture surface at all temperatures. Finally, the

BM shows two different failure modes as a function of temperature. At 20°C test temperatures, the fracture mode was found to be ductile with the presence of dimples at the fracture surface — Fig 7G. Mostly ductile with small brittle fracture surface was found at 0°C test temperature — Fig 7H. A brittle failure mode was found at -50°C where a cleavage fracture surface was identified, as shown in Fig. 7I.

Microhardness and Metallography

Microhardness of each weld at the bottom, middle, and top layer was measured to correlate with the strength of each weld zone. Figure 8A illustrates the hardness distribution for the friction stir weld region at the bottom layer, where the x direction is transverse to the weld direction. The hardness profiles along the two dashed lines in Fig. 8A are further plotted in Fig. 8B. The average measured hardness of the BM was approximately 170 HV. For the HAZ, the measured Vickers hardness value ranged from 175 to 185 HV. In the SZ, the highest hardness ranges from 195 to 220 HV. Similar hardness values were measured at the middle and top layer. Based on the hardness values in the SZ, it is expected that a bainitic microstructure formed upon cooling. Variations in hardness results are likely due to differences in the grain size and microstructures sampled by indentation grids. The hardness variation is fairly small between the different weld zones in MM-FSW when compared to a multipass flux cored arc welded pipe steel (X-80) where hardness variations up to 200 HV are common (Ref. 25). Moon et al. (Ref. 26) also used multipass gas metal arc welding (GMAW) on HSLA-100 steel with various heat inputs ranging from 1200 to 4300 kJ·m⁻¹. They found the hardness of the weldment varied from 199 to 400 HV and was greatly dependent on heat input and cooling rate.

One of the advantages of FSW is achieving high strength in the weld through grain refinement in the stir zone. However, due to the complexity of refined ferrite grains in the stir region, it is difficult to quantify grain

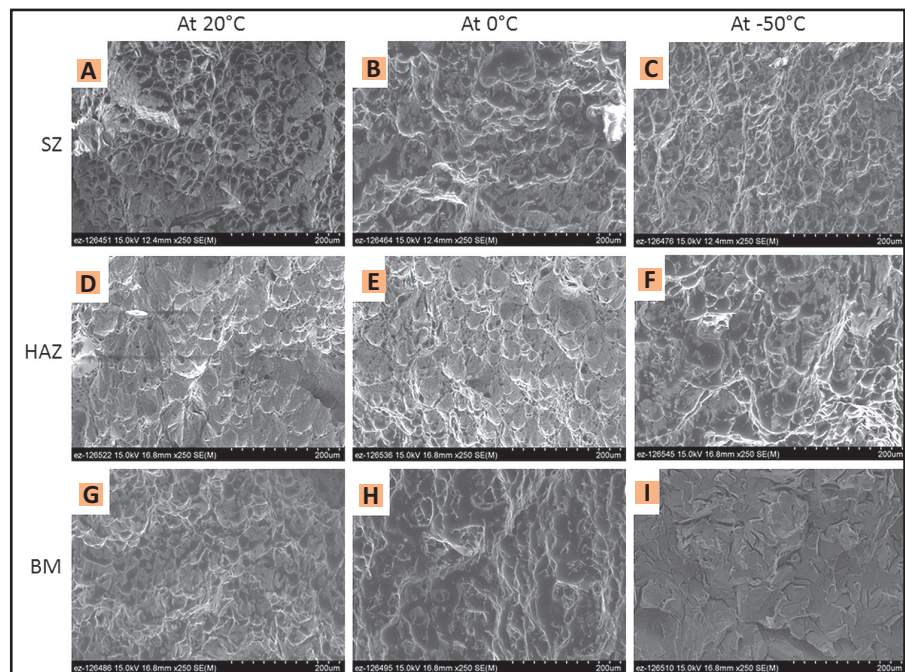


Fig. 7 — SEM images showing fracture surfaces after Charpy V-notch impact toughness testing (SZ, HAZ, and BM samples at the bottom layer) at different temperatures.

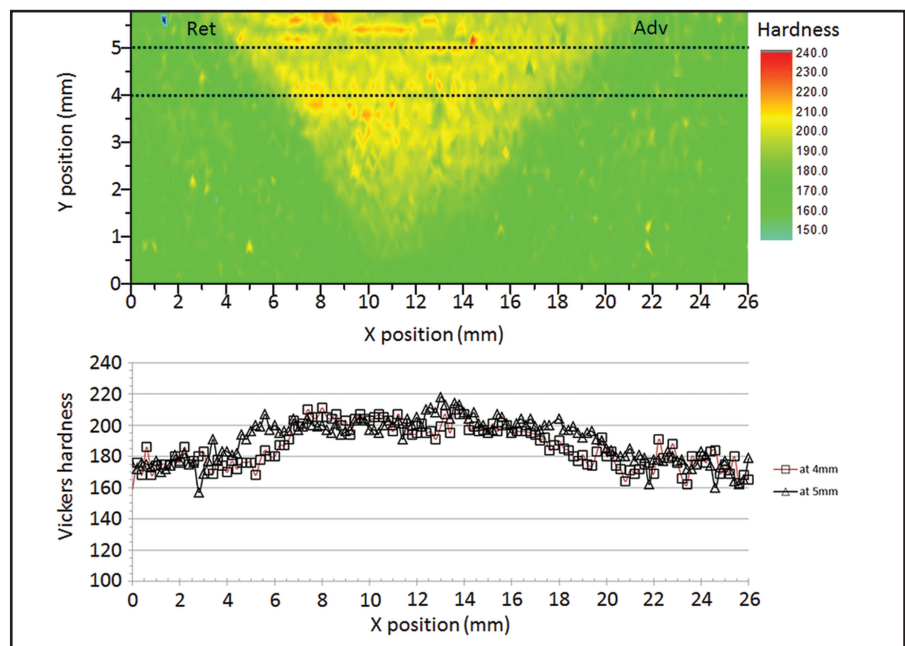


Fig. 8 — A — Mapped Vickers microhardness values for the bottom layer (butt joint) weld area; B — cross-sectional hardness plots at the height of 4 and 5 mm locations [dashed line in A]. (Adv: advancing side, Ret: retreating side) (Ref. 14).

size using optical microscopy and secondary electron microscopy. The current study applied EBSD to study the microstructures and grains of the friction stir welds. EBSD maps for the SZ, HAZ and unaffected BM are shown in Fig. 8. The base metal orientation map

(Fig. 9C) shows large polygonal ferrite with small islands of pearlite similar to that shown in Fig. 1. Significant grain refinement was found in the SZ (Fig. 9A), as compared with the BM — Fig. 9C. Grain refinement has been observed previously in the SZ due to dy-

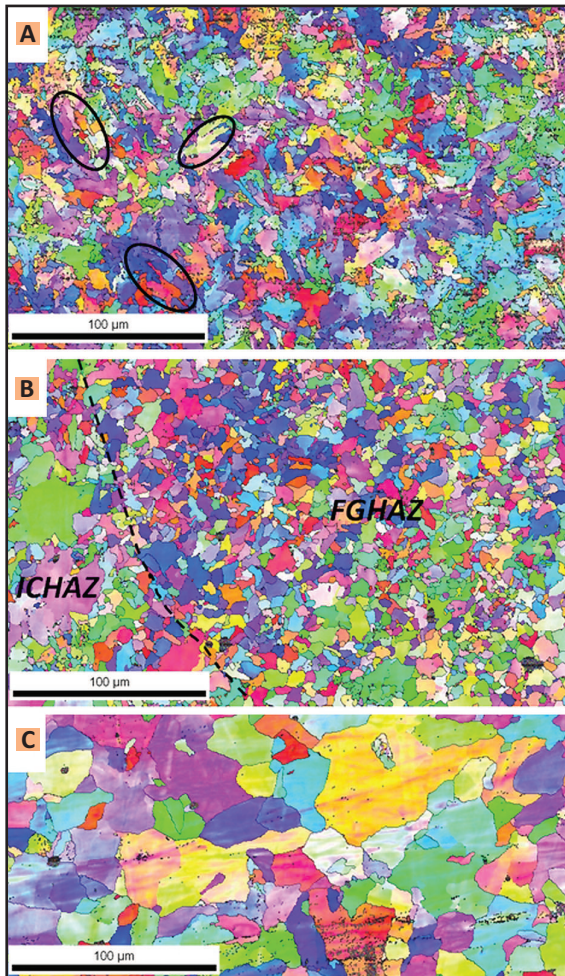


Fig. 9 — EBSD maps of different weld zones. A — Stir zone (some bainite plates were pointed out); B — heat-affected zone [Note: fine-grained heat-affected zone (FGHAZ) and intercritical heat-affected zone (ICHAZ)]; C — unaffected base metal.

dynamic recrystallization and severe plastic deformation during FSW (Ref. 1). In the SZ, the grains are not equiaxed. Wedge-shaped plate features, which are an indication of a bainitic microstructure, were also observed (Ref. 27). The hardness measured in the SZ ranged from 195 to 220 HVN, showing agreement with the microstructure observations.

During FSW, heat generation is influenced by the tool rotation rate and weld travel speed as well as material properties. Due to the difficulty of temperature measurements in the SZ, the empirical expression developed by Arbegast (Ref. 28) is used to estimate the peak temperature in the weld nugget.

nations of α and K values, the estimated peak temperature ranged from 1147° to 1433°C, which is lower than the liquidus temperature of steel. When α and K are 0.04 and 0.65, respectively, the calculated peak temperature is 1133°C. This estimated peak temperature is in reasonable agreement with the peak temperature (ranged from 1000° to 1200°C) reported by previous researchers (Refs. 1, 8). Similarly, Ghosh et al. (Refs. 29, 30) used Equation 1 to estimate the peak temperature (calculated ranged from 1030° to 1090°C) at the weld nugget for friction stir welded M190 steel. This estimated peak temperature in the SZ was well above the A_3 temperature of the steel, 824°C, which was calculated using *Thermo-Calc*® and

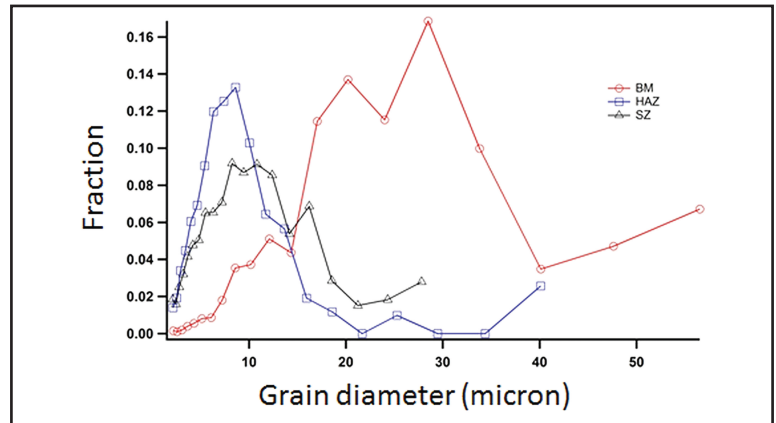


Fig. 10 — Grain size distribution of all three regions (SZ, HAZ, and BM).

$$\frac{T}{T_m} = K \left[\frac{\omega^2}{V \cdot 10^4} \right]^\alpha$$

(1) where T is the temperature during welding (°C), T_m is the liquidus temperature of the alloy (°C), ω is the tool rotational rate, V is the weld travel speed, α (range of 0.04–0.06) and K (range of 0.65–0.75) are two empirical material constants, respectively. The liquidus of A572 Grade 50 steel is about 1504°C (2740°F) and the transverse tool speed used in the experiment was $1.27 \times 10^{-3} \text{ m}\cdot\text{s}^{-1}$. The tool rotation speed was 250 rev/min (26.18 radian·s⁻¹).

TCFE database (Ref. 31). Therefore, for the stir zone, it is expected that the base metal mixture of ferrite and pearlite transforms to single-phase austenite during the heating cycle. Furthermore, the estimated peak temperature in the SZ supports the postulated peak temperature in the intercritical temperature range experienced by the HAZ.

The highest temperature, which is estimated about 1100°C based on the above calculation, can be used to explain the two distinct regions observed in the HAZ, i.e., the intercritical HAZ (ICHAZ) and the fine-grained HAZ (FGHAZ) shown in Fig. 9B.

In the ICHAZ, there coexists fine and coarse ferrite grains. The peak temperature experienced by this region during welding is between A_1 and A_3 . As a result, the ferrite to austenite transformation during heating is incomplete due to the low peak temperature, producing fragmented and thus smaller austenite grains mixed with original ferrite grains. Upon cooling, the austenite transforms back into ferrite, resulting in a microstructure in this region that is composed of newly formed fine ferrite surrounded by untransformed ferrite (Ref. 32).

On the other hand, the FGHAZ experiences a local peak temperature that is above A_3 , thus producing a full austenite microstructure albeit with smaller grain size than the parent ferrite upon heating (Ref. 27). However, as the highest temperature in the entire weld is capped at 1100°C, the austenite grain growth was limited in the FGHAZ. The small austenite trans-

forms back into ferrite during cooling, resulting in a final microstructure that is composed of fine ferrite grains. In addition, the kernel average misorientation (KAM), a parameter that is used to evaluate the strain or the stored energy for a given point (Refs. 33–35), shows a very small value and no significant preferred orientation for regions in Fig. 9B. Therefore, it is believed that this region is not significantly influenced by the mechanical deformation common to the thermal mechanically affected zone.

Figure 10 shows the grain size distribution in the SZ, HAZ (both FGHAZ and ICHAZ) and BM from EBSD data for the bottom layer. The average grain sizes of the FGHAZ and ICHAZ are slightly lower than that of SZ, both of which are less than 10 μm . As a result, the peak temperature of the FGHAZ observed in the current EBSD study is expected to be lower than 1000°C (Ref. 36). Conversely, the BM has the largest grain size, i.e., $\sim 30 \mu\text{m}$. Similar grain sizes and microstructures were found in the SZ, HAZ, and BM for the middle and top layers. For brevity, those microstructures are not repeated in the current paper.

Finally, the grain size was different in the SZ, HAZ, and BM with the smallest grain size found in the HAZ. If average grain diameters (9 μm for the HAZ, 10 μm for the SZ and 28 μm for the BM) were plugged into the following Hall-Petch relationship,

$$\sigma_g = K_y D^{-1/2} \quad (2)$$

where K_y is 0.363 MPa $\text{m}^{1/2}$ (Ref. 36), σ_g is the strength contribution from grain boundaries, and D is average grain diameter. The estimated strength contribution from grain boundaries for the SZ, HAZ, and BM are 114.8, 121, and 68.6 MPa, respectively. Since bainite, which has more dislocations than ferrite, is also observed in the SZ, additional strength in the SZ is expected. Nevertheless, the grain boundary strengthening has a significant effect in the current friction stir weld. Additionally, a refinement in grain size can increase the impact toughness.

By taking advantage of the MM-FSW method, a potential application for the present work could be fabrication of multilayer high-pressure stor-

age vessels. Multilayer pressure vessels or storages are often preferred over heavy thick single-wall structures due to lower cost and manufacturing efficiency (Refs. 37, 38).

Conclusion

In conclusion, the use of MM-FSW enables fabrication of thick structures in high-strength low-alloy steel. This technique can be potentially used for multilayer high-pressure storage/vessel applications. Strengths in the SZ and HAZ were higher than the BM based on microhardness measurements. Also, CVN results indicate that impact toughness in the SZ and HAZ are generally higher than BM. Both the SZ and HAZ have fine-grained microstructures, although the mechanism for it is expected to be different for the SZ (i.e., dynamic recrystallization) vs. the HAZ (i.e., intercritical temperature). Taken together, with all the mechanical tests and hardness measurements, the present work indicates that the overall mechanical strength of the MM-FSW steel samples were comparable or superior to the base metal. For future work, hooking that occurs due to the butt/lap joint configuration should be avoided by either using a special tool to produce horizontal metal flow or by using an alternate joint design.

Acknowledgments

The authors would like to acknowledge the financial support of the U.S. Department of Energy Office of Energy Efficiency and Renewable Energy, Fuel Cell Technologies Office and Advanced Manufacturing Office. Oak Ridge National Laboratory (ORNL) is managed by UT-Battelle, LLC, for the U.S. Department of Energy under Contract DE-AC05-00OR22725.

References

- Lienert, T. J., Stellwag, W. L., Grimmett, B. B. Jr., and Warke, R. W. 2003. Friction stir welding studies on mild steel — Process results, microstructures, and mechanical properties are reported. *Welding Journal* 82(1): 1-s to 9-s.

- Dawes, C. J., and Thomas, W. M. 1996. Friction stir process welds aluminum alloys. *Welding Journal* 75(3): 41-s to 45-s.

- Yu, Z. Z., Zhang, W., Choo, H., and Feng, Z. 2012. Transient heat and material flow modeling of friction stir processing of magnesium alloy using threaded tool. *Metallurgical and Materials Transactions A: Physical Metallurgy and Materials Science* 43A (2): 724 to 737.

- Woo, W., Balogh, L., Ungar, T., Choo, H., and Feng, Z. 2008. Grain structure and dislocation density measurements in a friction-stir welded aluminum alloy using X-ray peak profile analysis. *Materials Science and Engineering A- Structural Materials Properties Microstructures and Processing* 498(1–2): 308 to 313.

- Park, H. S., Kimura, T., Murakami, T., Nagano, Y., Nakata, K., and Ushio, M. 2004. Microstructures and mechanical properties of friction stir welds of 60% Cu-40% Zn copper alloy. *Materials Science and Engineering A- Structural Materials Properties Microstructures and Processing* 371 (1–2): 160 to 169.

- Rai, R., De, A., Bhadeshia, H. K. D. H., and DebRoy, T. 2011. Review: friction stir welding tools. *Science and Technology of Welding and Joining* 16(4): 325 to 342.

- Park, S. H. C., Sato, Y. S., Kokawa, H., Okamoto, K., Hirano, S., and Inagaki, M. 2003. Rapid formation of the sigma phase in 304 stainless steel during friction stir welding. *Scripta Materialia* 49(12): 1175 to 1180.

- Thomas, W. M., Threadgill, P. L., and Nicholas, E. D. 1999. Feasibility of friction stir welding steel. *Science and Technology of Welding and Joining* 4(6): 365 to 372.

- Fujii, J., Cui, L., Tsuji, N., Maeda, M., Nakata, K., and Nogi, K. 2006. Friction stir welding of carbon steels. *Materials Science and Engineering A- Structural Materials Properties Microstructures and Processing* 429(1-2): 50 to 57.

- Khodir, S. A., Morisada, Y., Uejii, R., and Fujii, H. 2012. Microstructures and mechanical properties evolution during friction stir welding of SK4 high carbon steel alloy. *Materials Science and Engineering A- Structural Materials Properties Microstructures and Processing*. 558: 572 to 578.

- Taendl, J., Nambu, S., Inoue, J., Enzinger, N., and Koseki, T. 2012. Friction stir welding of multilayered steel. *Science and Technology of Welding and Joining*. 17(3): 244 to 253.

- Matsushita, M., Kitani, Y., Ikeda, R., Endo, S., and Fujii, H. 2012. Microstructure and toughness of friction stir weld of thick structural steel. *ISIJ International*. 52(7): 1335 to 1341.

- Feng, Z., David, S. A., and Frederick, D. A. 2010. Multiple pass and multiple

layer friction stir welding and material enhancement processes. U.S. patent 7762447.

14. Lim, Y. C., Sanderson, S., Mahoney, M., Qiao, D., Wang, Y., Zhang, W., and Feng, Z. 2013. *Mechanical Properties and Microstructural Characterization of a Multi-layered Multipass Friction Stir Weld in Steel. Friction Stir Welding and Processing VII*. eds R. Mishra, M. W. Mahoney, Y. Sato, Y. Hovanski, and R. Verma. pp. 81–90. John Wiley & Sons, Inc., Hoboken, N.J.

15. Brown, R., Tang, W., and Reynolds, A. P. 2009. Multi-pass friction stir welding in alloy 7050-T7451: Effects on weld response variables and on weld properties. *Materials Science and Engineering A- Structural Materials Properties Microstructures and Processing* 513-14: 115 to 121.

16. Badarinarayan, H., Yang, Q., and Zhu, S. 2009. Effect of tool geometry on static strength of friction stir spot-welded aluminum alloy. *International Journal of Machine Tools & Manufacture* 49(2): 142 to 148.

17. Ericsson, M., Jin, L. Z., and Sandstrom, R. 2007. Fatigue properties of friction stir overlap welds. *International Journal of Fatigue* 29(1): 57 to 68.

18. Badarinarayan, H., Shi, Y., Li, X., and Okamoto, K. 2009. Effect of tool geometry on hook formation and static strength of friction stir spot welded aluminum 5754-O sheets. *International Journal of Machine Tools & Manufacture* 49(11): 814 to 823.

19. Yin, Y. H., Sun, N., North, T. H., and Hu, S. S. 2010. Influence of tool design on mechanical properties of AZ31 friction stir spot welds. *Science and Technology of Welding and Joining* 15(1): 81 to 86.

20. Yadava, M. K., Mishra, R. S., Chen, Y. L., Carlson, B., and Grant, G. J. 2010. Study of friction stir joining of thin aluminum sheets in lap joint configuration. *Science and Technology of Welding and Joining*. 15(1): 70 to 75.

21. Fuller, C. B., Mahoney, M. W., and Bingel, W. H. 2005. Friction Stir Weld Tool and Method. U.S. Patent 20050121497 A1.

22. Konkol, P. J., and Mruzeczek, M. F. 2007. Comparison of friction stir weldments and submerged arc weldments in HSLA-65 steel. *Welding Journal* 86(7): 187-s to 195-s.

23. Arora, K. S., Pandey, S., Schaper, M., and Kumar, R. 2010. Microstructure Evolution during friction stir welding of aluminum alloy AA2219. *Journal of Materials Science & Technology* 26 (8): 747 to 753.

24. Mochizuki, M., Inuzuka, M., Nishida, H., Nakata, K., and Toyoda, M. 2006. Fracture toughness of structural aluminum alloy thick plate joints by friction stir welding. *Science and Technology of Welding and Joining* 11(3): 366 to 370.

25. Song, H. Y., Zhang, W., Babu, S. S., and Feng, Z. 2013. Toward understanding of mechanical property degradation of steel welds in high-pressure hydrogen transmission pipeline — Role of microstructure. *Proceedings of the 9th International Conference on Trends in Welding Research*. Eds. DebRoy, T., S. A. David, J. N. Koseki, and H. K. Bhadeshia. pp. 461–468. ASM International.

26. Moon, D. W., Fonda, R. W., Spanos, G. 2000. Microhardness variations in HSLA-100 welds fabricated with new ultra-low-carbon weld consumables. *Welding Journal* 79(10): 278-s to 285-s.

27. Bhadeshia, H. K. D. H. 2001. *Bainite in Steels: Transformations, Microstructures and Properties*, IOM Communication Ltd., London, pp.19.

28. Arbegast, W. J., in: Z. Jin, A. Beau-doin, T. A. Bieler, B. Radhakrishiman (Eds.), *Hot Deformation of Aluminum Alloys III*, TMS, San Diego, Calif., 2003, pp. 313–327.

29. Ghosh, M., Kumar, K., and Mishra, R. S. 2010. Analysis of microstructural evolution during friction stir welding of ultrahigh-strength steel. *Scripta Materialia* 63(8): 851 to 854.

30. Ghosh, M., Kumar, K., and Mishra, R. S. 2011. Friction stir lap welded advanced high strength steels: Microstructure and mechanical properties. *Materials Science and Engineering A- Structural Mate-*

rials Properties Microstructures and Processing 528(28): 8111 to 8119.

31. www.thermocalc.com/start/

32. Zhang, W., Elmer, J. W., and DebRoy, T. 2002. Modeling and real time mapping of phases during GTA welding of 1005 Steel. *Materials Science and Engineering A — Structural Materials Properties Microstructures and Processing*. 333(1-2): 320 to 335.

33. Bingert, J. F., Livescu, V., Cerreta, and E. K., in: A. J. Schwartz, M. Kumar, B. L. Adams (Eds.), *Electron Backscatter Diffraction in Materials Science*, 2nd Ed., Springer, New York, N.Y., 2009, pp. 301–315.

34. Khan, A. S., Baig, M., Choi, S. H., Yang, H. S., and Sun, X. 2012. Quasi-static and dynamic responses of advanced high strength steels: Experiments and modeling. *International Journal of Plasticity*, 30–31: 1 to 17.

35. Badji, R., Chauveau, T., and Bacroix, B. 2013. Texture, misorientation and mechanical anisotropy in a deformed dual phase stainless steel weld joint. *Materials Science and Engineering A- Structural Materials Properties Microstructures and Processing* 515: 94 to 103.

36. Yu, X., Caron, J. L., Babu, S. S., Lippold, J. C., Isheim, D., and Seidman, D. N. 2010. Characterization of microstructural strengthening in the heat-affected zone of a blast-resistant naval steel. *Acta Materialia* 58 (17): 5596 to 5609.

37. Zhen, L., Jiang, N., and Liu, S. J. 2011. Experimental study of integrated multilayer clamping high pressure vessel. *Journal of Pressure Vessel Technology-Transactions of the ASME* 133(6): 061206-1 to 061206-6.

38. Zhang, W., Ren, F., Feng, Z., Wang, J.-A., Jawad, M., Kelly, M., and Vossoughi, F. 2012. Design analysis of steel concrete composite vessel for stationary storage of high-pressure hydrogen. *International Hydrogen Conference: Hydrogen-Materials Interactions*. Eds. B. P. Somerday and P. Sofronis, pp. 479–488. ASME.

Call for Presentations National Robotic Arc Welding Conference

The National Robotic Arc Welding Conference will take place June 1–3, 2015, in Milwaukee, Wis. This year's theme is "Future Tools — Future Workforce" in recognition of the fact that new technology will not work well without trained and motivated people.

We are looking for speakers who have addressed robotic and automatic arc welding-related challenges and succeeded through innovation in part design, tooling, process optimization, workforce training, or other means. Submissions are welcomed from end users, equipment suppliers, or a combination of both. If you are interested, please submit

your presentation title, short paragraph discussing what it is about, and who will give the 30-min talk to j.noruk@servorobot.com. Deadline for consideration is December 31, 2014.

This premier conference traces its roots to 1983 when John Hinrichs, who passed away in 2012, started it with the purpose of helping the fledgling robotic welding industry grow by sharing new technology and ideas. Proceeds from the conference will go to the John Hinrichs Memorial Endowment, which is currently funded in an amount to provide more than \$10,000 annually in scholarships.